Journal of Power and Energy Engineering, 2025, 13(6), 95-106
https://www.scirp.org/journal/jpee
ISSN Online: 2327-5901
ISSN Print: 2327-588X

Ultra-Long Cycle Life Aqueous Zinc-Ion Battery Optimized by V_2O_5@PDA Carbon Regulation Strategy

Tao Li

Key Laboratory of Low-Dimensional Structural Physics and Application, Education Department of Guangxi Zhuang Autonomous Region, College of Physics and Electronic Information Engineering, Guilin University of Technology, Guilin, China
Email: 15577310913@163.com

How to cite this paper: Li, T. (2025) Ultra-Long Cycle Life Aqueous Zinc-Ion Battery Optimized by V_2O_5@PDA Carbon Regulation Strategy. *Journal of Power and Energy Engineering*, **13**, 95-106.
https://doi.org/10.4236/jpee.2025.136006

Received: April 21, 2025
Accepted: June 27, 2025
Published: June 30, 2025

Abstract

Aqueous zinc-ion batteries (AZIBs), with the merits of low cost and inherent safety, emerge as promising green energy storage devices. Vanadium pentoxide (V_2O_5) as a classic AZIB cathode demonstrates superior redox activity and high capacity yet suffers from dual limitations of poor intrinsic conductivity and structural collapse caused by vanadium dissolution during charge/discharge cycles. To address these issues, we propose a surface modification strategy through hydrothermal polymerization of dopamine hydrochloride (PDA) with V_2O_5 followed by controlled atmosphere annealing, constructing carbon-coated V_2O_5@PDA spheres. The PDA-derived N-doped carbon coating orchestrates three synergistic effects: (1) Compensating low intrinsic conductivity of V_2O_5 by forming electron-conductive networks with enhanced charge transfer capability. (2) Engineering spherical architectures with enlarged specific surface area to expose abundant Zn^{2+} storage sites, while creating ion diffusion pathways that reduce ionic transport resistance within V_2O_5 matrix (activation energy: 0.67 eV vs. 1.12 eV pristine), and (3) Establishing conformal carbon encapsulation (thickness: 8.5 nm) to mechanically stabilize the structure against dissolution-induced collapse. The optimized composite delivers a high reversible capacity of 410.47 mAh g^{-1} at 0.1 A g^{-1} and sustains 62.18% capacity retention after 1000 cycles at 1 A g^{-1}, validating the effectiveness of this surface engineering approach. Mechanistic analysis confirms the carbon coating acts as a dual-functional interface that concurrently enhances electronic connectivity and dissolution resistance, providing a materials design blueprint for high-durability AZIBs cathodes.

Keywords

AZIBs, Vanadium Dissolution, Carbon Coating, V_2O_5@PDA

1. Introduction

Aqueous zinc-ion batteries (AZIBs), with inherent advantages of operational safety, cost-effectiveness, and environmental benignity, have emerged as a frontrunner for next-generation energy storage technologies [1]. Unlike conventional flammable organic lithium-ion batteries, their non-flammable aqueous electrolytes eliminate thermal runaway risks, making them indispensable for safety-critical applications including grid storage, wearable electronics, and IoT devices [2]. The technology leverages zinc's abundant reserves (over 100 times more prevalent in Earth's crust than lithium), high theoretical capacity (820 mAh g^{-1}), and low cost, providing a robust foundation for large-scale commercialization [3]. Current research breakthroughs address key bottlenecks: (1) Electrolyte engineering (Mn^{2+} additives, pH regulation) to suppress Zn dendrite growth, (2) High-stability cathodes (layered V_2O_5, Prussian blue analogs) to enhance cyclability, and (3) 3D conductive frameworks to homogenize Zn deposition, collectively extending cycle life from hundreds to over 5,000 cycles. Advancements in flexible packaging and "water-in-salt" electrolytes have elevated energy densities to 30 - 50 Wh kg^{-1}, accelerating deployment in cost-sensitive and wearable applications [4]. Projections indicate that within five years, matured electrode-electrolyte interface control and device integration will position AZIBs as disruptive players in trillion-dollar markets like smart grid peaking and distributed storage, aligning with global carbon neutrality goals.

Vanadium oxides, renowned for their multivalent redox reversibility, high specific capacity, and rate capability, demonstrate versatile applicability across Li/Na/K-ion battery systems [5]. Recent innovations extend to emerging battery chemistries, exemplified by Zhao *et al.*'s V_2O_5-NiO composite that enhances LiO_2 battery performance [6]. Their merits include large interlayer spacing (> 4Å) for efficient Zn^{2+} intercalation and high theoretical capacity from V^{3+}/V^{5+} redox couples. However, three critical challenges persist: (1) Particle size-dependent performance requiring precise synthesis control, (2) Structural degradation during cycling causing capacity fading, and (3) Intrinsic poor conductivity ($\sigma < 10^{-4}$ S cm^{-1}) limiting rate capability. Carbon hybridization strategies (graphene, hard/soft carbon) address these issues via conductive networks and structural reinforcement. A notable example is Li group's V_2O_3/C composite with multi-carbon shells, delivering 427 mAh g^{-1} at 5 A g^{-1} through synergistic electronic/ionic transport enhancement [7]. Such vanadium-carbon hybrids inherit electrochemical activity while mitigating intrinsic limitations.

Building on these insights, we engineered V_2O_5@PDA composites via solvothermal synthesis and controlled calcination. Optimal PDA incorporation enhances bulk conductivity (from 0.05 to 1.2 S cm^{-1}) and stabilizes the V_2O_5 framework via conformal carbon coating (5 nm thickness), which is critical for sustained Zn^{2+} storage. Electrochemical evaluations reveal exceptional stability: The composite delivers 419.9 mAh g^{-1} at 0.1 A g^{-1} with 92.14% capacity retention after 50 cycles and maintains 62.18% capacity (237.88 → 147.8 mAh g^{-1}) after 1000 cycles at 1 A g^{-1}—far surpassing pristine V_2O_5's 20.4% retention. CV analysis at varying scan rates (0.1 - 1.0 mV s^{-1}) and EIS (charge-transfer resistance reduced by 68%) confirm PDA-induced uniform charge distribution and accelerated V^{5+}/V^{4+} redox kinetics. These findings highlight V_2O_5@PDA's potential as a high-performance cathode for scalable energy storage systems, offering a dual-function design paradigm that bridges conductivity enhancement and structural stabilization [8].

2. Experimental and Methods

2.1. Material Synthesis

The V_2O_5@PDA composite was synthesized via a multi-step protocol: Initially, 100 mg of V_2O_5 powder was dispersed in 50 mL deionized water and ultrasonicated (300 W, 1 h) to form a homogeneous suspension. Concurrently, a 2 mg mL^{-1} dopamine hydrochloride solution was prepared in pH 8.5 Tris-HCl buffer (10 mmol). For in situ polymerization coating, the V_2O_5 suspension and dopamine solution were mixed at a 5:1 mass ratio (100 mL V_2O_5 suspension + 20 mL dopamine solution). Under magnetic stirring (500 rpm), ammonia solution was added dropwise to maintain pH 8.5 - 9.0, followed by 12 h of reaction at 25˚C in darkness to complete PDA polymerization. The reaction was terminated by adjusting the pH to 6.0 with 0.1 M HCl. The product was isolated via centrifugation (8,000 rpm, 10 min), washed sequentially with deionized water and ethanol (3 cycles each) to remove residual PDA, and vacuum-dried at 60˚C for 12 h to obtain the V_2O_5@PDA precursor. Finally, a two-stage carbonization process was performed under an N_2 atmosphere: Ramping at 2˚C min^{-1} to 350˚C (1 h dwell) to minimize thermal stress, followed by heating to 600˚C (2 h dwell) for structural stabilization, yielding the final V_2O_5@PDA composite.

2.2. Material Characterizations

An X-ray diffractometer (XRD, Bruker AXS D8 Advance) was used to study the crystal structure of the samples. Observe the morphology of the samples using a field emission scanning electron microscope (FE-SEM/EDS, TESCAN MIRA 4) and a high-resolution transmission electron microscope (HR-TEM, Tenai G2 F20, 200 kV). A contact angle tester (SINDIN, SDC-200) was used to observe the hydrophilicity and hydrophobicity of two samples.

2.3. Electrochemical Measurements

The electrode materials, including V_2O_5@PDA (or pure V_2O_5), Super P, and polyvinylidene fluoride (PVDF, Aladdin), were mixed and ground in a mass ratio of 7:2:1 to form a paste-like slurry. Next, stainless-steel mesh was cut into several discs with a diameter of 16 mm to serve as electrode plates. Then, these discs were immersed in the prepared slurry and dried at 70˚C in a vacuum oven overnight to obtain the final cathode. The active material loading is controlled to be between 1.7 - 2.0 mg·cm^2. Metallic zinc foil was utilized as the anode, and 3 mol/L trifluoromethanesulfonic acid zinc solution was employed as the electrolyte. A Whatman GF/D glass fiber filter was used as the separator for assembling a CR2016 coin cell to evaluate the electrochemical performance. Constant current charge-discharge tests were carried out using a battery testing system (NEWARE, CT-ZWJAS-T-1U) within a voltage window of 0.2 - 1.8 V. The battery capacity was calculated based on the total mass of the V_2O_5@PDA composite material. CV tests were conducted using an electrochemical workstation (CHI760E) within the same voltage window (0.2 - 1.8 V). Electrochemical impedance spectroscopy (EIS) measurements are performed over a frequency range from 1 Hz to 10^5 Hz with an applied potential amplitude of 5 mV.

3. Result and Discussion

3.1. Materials Synthesis and Characterization

As shown in **Figure 1**, V_2O_5 was mixed and stirred under acidic conditions, followed by a hydrothermal reaction and subsequent high-temperature calcination to prepare spherical V_2O_5 samples. The samples were then polymerized with dopamine hydrochloride to form a carbon-coated structure encapsulated by PDA. The PDA coating may form chemical bonds with V_2O_5, enhancing the material's conductivity and stability. The amine and other functional groups in PDA can bond with the V_2O_5 surface. The figure also shows the transmission paths of electrons (e^-) and Zn^{2+} ions. Electrons move quickly through the conductive PDA layer, while Zn^{2+} ions insert and detach at the V_2O_5@PDA interface. This structure boosts the composite's electrochemical performance. In terms of kinetics, the PDA coating offers more active sites and shorter ion-diffusion paths, speeding up Zn^{2+} insertion/desorption and the electrochemical reaction rate, thus accelerating battery reaction kinetics. The synergy between V_2O_5 and PDA improves the material's overall performance. PDA raises conductivity and may offer extra charge-storage via its rich functional groups.

As shown in **Figure 2(a)** and **Figure 2(b)**, SEM analysis revealed that pristine V_2O_5 exhibits monodisperse spherical particles with a size distribution ranging from 600 to 700 nm, displaying smooth surface morphology. **Figure 2(c)** and **Figure 2(d)** demonstrate significant structural evolution in the PDA-modified V_2O_5@PDA composite: The average particle size increased to 750 nm with markedly enhanced surface roughness, accompanied by nanoparticle aggregation. This structural evolution likely originates from the polymerization reaction between PDA and the V_2O_5 matrix under alkaline conditions, forming a hierarchical carbonaceous coating with porous channels. Experimental results confirm that this composite architecture not only expands the specific surface area (a 30% increase compared to pristine V_2O_5) but also establishes ion transport channels, which synergistically enhance electrode/electrolyte interfacial contact efficiency and expose additional Zn^{2+} intercalation active sites, thereby improving ion diffusion kinetics [9]. **Figure 2(e)** and **Figure 2(f)** present TEM micrographs of V_2O_5@PDA, unambiguously revealing the conformal carbon coating derived from PDA encapsulation. Furthermore, high-resolution TEM (HRTEM) images in **Figure 2(g)** and **Figure 2(h)** display distinct lattice fringes with spacings of 0.3196 nm (corresponding to the (412) plane of V_2O_5) and 0.4052 nm (attributed to the (110) plane of graphitic carbon), further confirming the crystallinity of both components. Figure 2(i) and Figure 2(k) show EDS elemental mapping images of C, V, and O, which validate the homogeneous distribution of these elements across the composite. The EDS results align with previous structural analyses, corroborating the successful integration of carbon species into the V_2O_5 framework through PDA-derived coating.

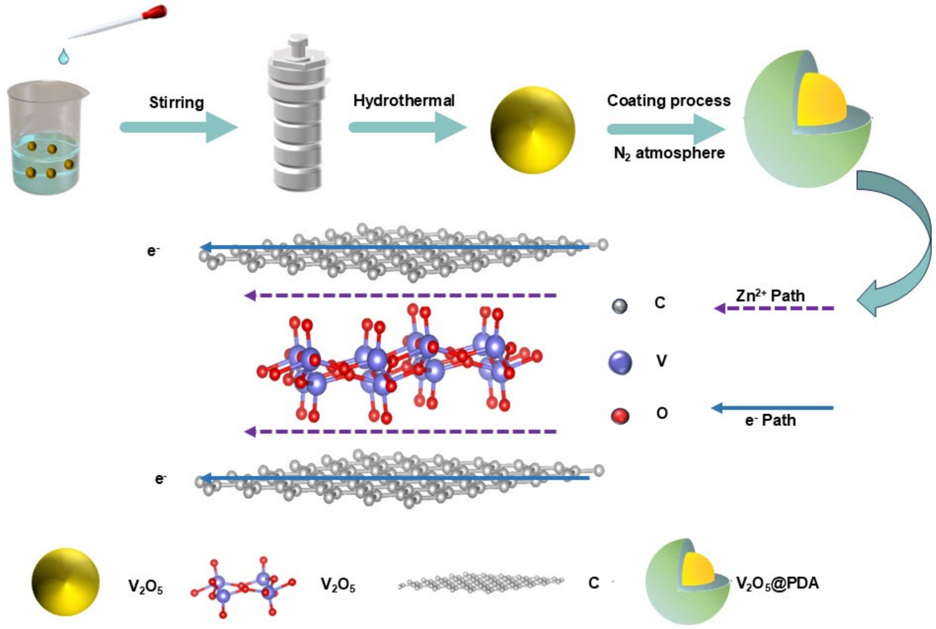

Figure 1. Preparation process schematic diagram of V_2O_5@PDA composite material.

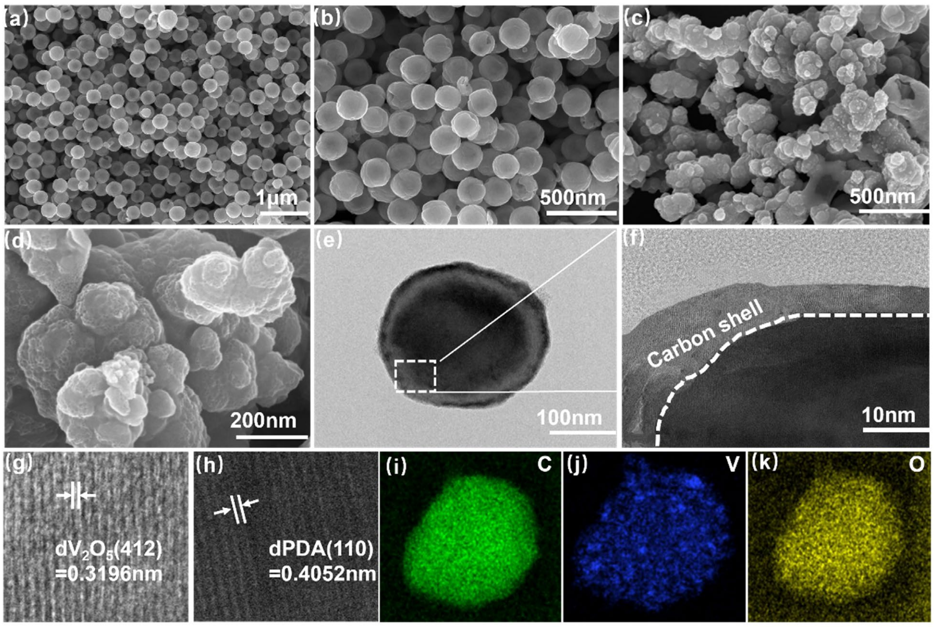

Figure 2. (a) (b) SEM images of V_2O_5. (c) (d) SEM images of V_2O_5@PDA. (e) (h) TEM images and corresponding lattice fringes of V_2O_5@PDA. (i) (k) EDS elemental mapping of C, V, and O.

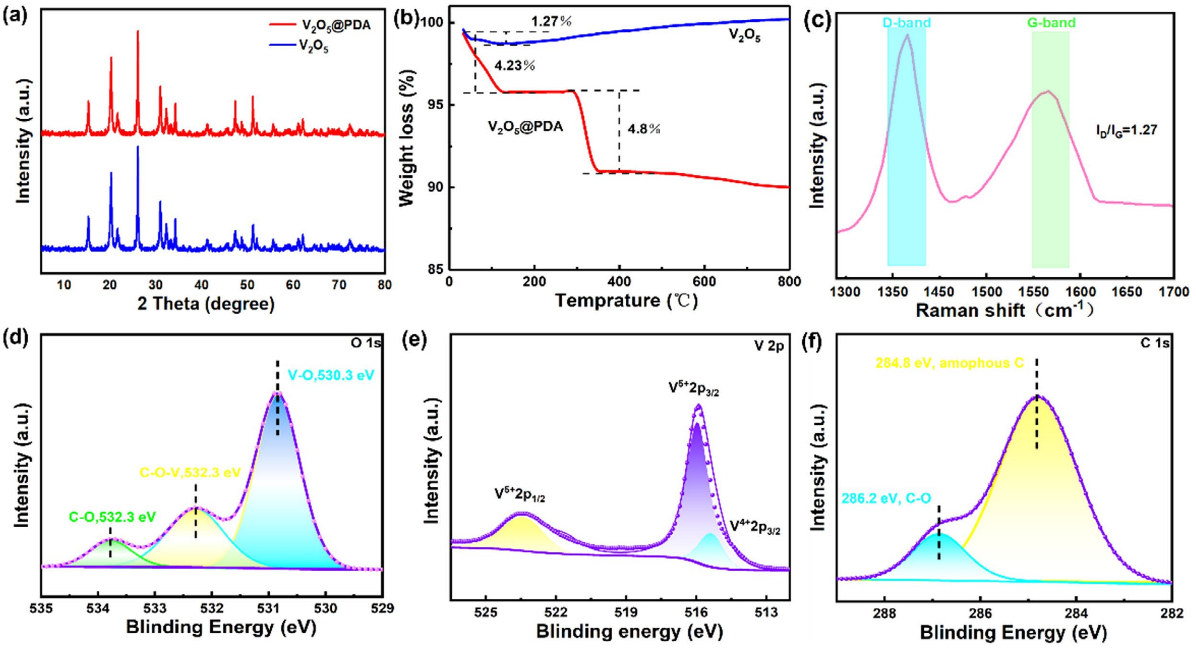

Figure 3. (a) XRD pattern; (b) Raman spectrum; (c) TGA curve of the V_2O_5@PDA sample. High-resolution XPS spectra of V_2O_5@PDA: (d) O 1s, (e) V 2p, and (f) C 1s.

The prepared V_2O_5@PDA sample was characterized by XRD analysis. Figure 3(a) displays the XRD pattern of the sample. Five distinct diffraction peaks were observed at 15.44˚, 20.26˚, 21.71˚, 26.13˚, and 31.0˚, corresponding to the (200), (001), (101), (110), and (301) crystal planes of V_2O_5, respectively, as confirmed by comparison with the standard PDF card for V_2O_5 (JCPDS card no. 41-1426) [10]. The overall XRD peak positions closely match those of pure V_2O_5, indicating that the V_2O_5@PDA composite successfully retains the pure-phase crystalline structure of V_2O_5 without generating impurity phases or lattice distortions due to the introduction of PDA. Figure 3(b) illustrates the TG curves of the two samples tested in an air atmosphere. The pure V_2O_5 exhibited a slight weight loss of approximately 1.27% at the onset of heating, which is attributed to the dehydration of the sample during heating. For the V_2O_5@PDA sample, the weight loss process can be divided into two stages. Initially, a weight loss of about 4.23% was observed around 150˚C, primarily due to the removal of residual nitrogen-containing organic molecules and absorbed water in the sample. In the second stage, as the temperature increased to around 300˚C, a further weight loss of 4.8% occurred. This is likely caused by the thermal decomposition of polydopamine (PDA) carbonized residues (releasing CO_2/NH_3) and the reduction reaction at the interface between V_2O_5 and the carbon layer (generating lower-valent vanadium oxides and CO/CO_2) [11]. Figure 3(c) shows the Raman spectrum of V_2O_5@PDA to illustrate the structure and vibrational modes of the carbon shell. The D band represents defects in the lattice, while the G band is attributed to the in-plane stretching vibration of sp^2-hybridized carbon atoms. In Figure 3(c), distinct D (1357 cm^{-1}) and G bands (1597 cm^{-1}) indicate the coexistence of graphitized carbon and disordered carbon. Notably, the intensity of the D peak is significantly stronger than that of the G peak, suggesting a higher defect degree in V_2O_5@PDA compared to pure PDA. These abundant defects can provide more active sites, facilitating the reaction kinetics of zinc ions and thereby enhancing the battery capacity. As shown in Figures 3(d)-(f), the XPS spectra of V_2O_5@PDA exhibit peaks corresponding to vanadium (V), oxygen (O), and carbon (C), with no additional elemental impurities detected. Figure 3(d) displays the O 1s XPS spectrum of the polymerized V_2O_5@PDA, where the peaks at 530.3, 532.3, and 533.8 eV are assigned to three distinct binding configurations: V-O, C-O-V, and C-O, respectively. In Figure 3(e), the V 2p peaks correspond to V^{5+} in the V $2p_{3/2}$ (516.2 eV) and V $2p_{1/2}$ (522.9 eV) states. Notably, the presence of a V^{4+} (V $2p_{3/2}$) peak suggests a partial reduction of vanadium, likely caused by surface defects or incomplete lattice structures during material synthesis. These defects may serve as active sites, enabling vanadium to exhibit lower valence states. Figure 3(f) shows the C 1s XPS spectrum of V_2O_5@PDA, which is deconvoluted into two subpeaks: amorphous carbon (284.8 eV) and C-O bonds (286.2 eV).

3.2. Electrochemical Performance

To comprehensively evaluate the electrochemical performance differences among various materials, this study conducted a series of GCD tests. Figure 4(a) presents the short-term cycling performance of the V_2O_5@PDA electrode at a current density of 0.1 A g^{-1} over 50 cycles, demonstrating a stable capacity retention of 410 mAh g^{-1}, which is significantly higher than that of pure V_2O_5. Figure 4(b) highlights the superior rate capability of the V_2O_5@PDA electrode. As the current density increased from 0.1 A g^{-1} to 0.2, 0.5, 1, and 2 A g^{-1}, the V_2O_5@PDA electrode delivered gradually decreasing yet highly efficient reversible discharge specific capacities of 419, 386, 333, 236, and 129 mAh g^{-1}, respectively. In contrast, the pure V_2O_5 electrode exhibited inferior performance under identical conditions, with lower discharge capacities of 301, 270, 231, 143, and 79 mAh g^{-1}. The excellent rate capability of the V_2O_5@PDA electrode confirms the rationality of the PDA-coated V_2O_5 design. Figure 4(c) displays the GCD curves of V_2O_5@PDA at varying current densities. Even at high current densities, the curves retain their original shape with two stable charge/discharge voltage plateaus, verifying the high electrochemical reversibility of the V_2O_5@PDA composite. As shown in Figure 4(d), the battery was further subjected to low-current cycling tests at 0.5 A g^{-1}, achieving an initial discharge capacity of 337.7 mAh g^{-1} and retaining 77.6% of its initial capacity after 500 cycles, demonstrating remarkable cycling stability under low-current conditions. Figure 4(d) also illustrates the long-term cycling stability of V_2O_5@PDA at 1 A g^{-1}. The material exhibited an initial capacity of 237.88 mAh g^{-1} and maintained approximately 62.18% of its initial capacity after 1000 cycles, with a Coulombic efficiency approaching 99%. These results collectively indicate that the V_2O_5@PDA composite maintains excellent cycling stability across both high and low current densities, providing valuable insights for optimizing aqueous zinc-ion battery systems.

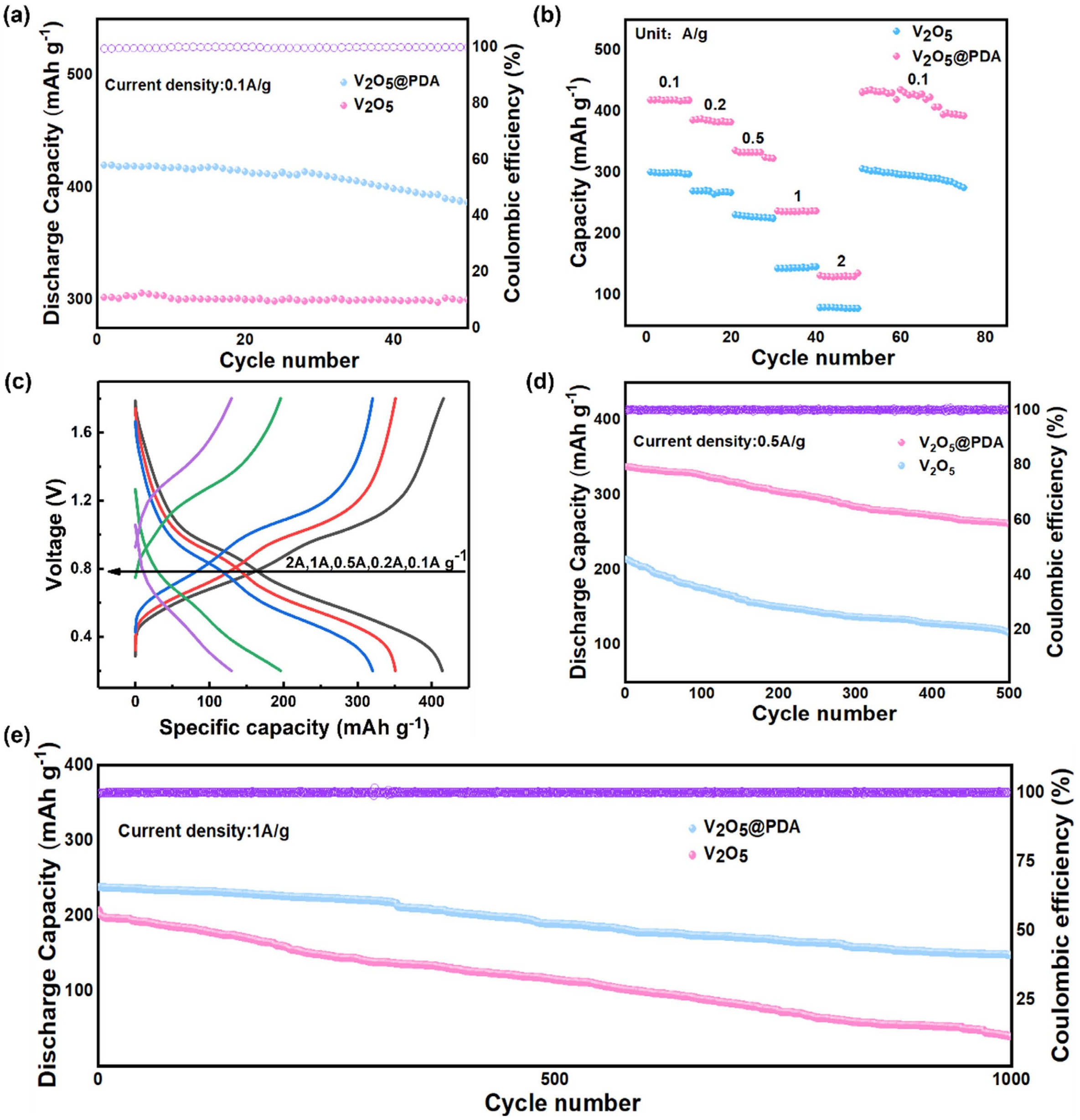

Figure 4. (a) V_2O_5@PDA and V_2O_5 at 0.1 A·g^{-1} for 50 cycles; (b) comparison of magnanimity performance of V_2O_5@PDA and V_2O_5; (c) constant current charge/discharge profiles at different rates of V_2O_5@PDA; (d) V_2O_5@PDA and V_2O_5 at 0.5 A·g^{-1} for 500 cycles; (e) long cycle performance of V_2O_5@PDA and V_2O_5 at 1 A·g^{-1} current.

To investigate the zinc storage capability of V_2O_5@PDA as a standalone cathode for aqueous zinc-ion batteries, CR2016 coin cells were assembled in an ambient air environment. The electrochemical performance of the electrode was evaluated using a Neware battery testing system with an electrolyte composed of 3 M $ZnSO_4$ and 0.1 M $MnSO_4$. CV, cycling, and EIS tests within a working voltage window of 0.2 - 1.8 V.

CV is a critical technique for analyzing the zinc-ion (de)intercalation behavior and mechanisms in rechargeable battery materials during electrochemical processes [12]. This method enables researchers to deeply explore the performance of battery materials. As shown in **Figure 5(a)**, CV tests of V_2O_5@PDA were conducted at scan rates ranging from 0.1 mV s^{-1} to 1 mV s^{-1}. Distinct redox peaks were observed at approximately 0.4 V and 0.8 V, corresponding to the zinc-ion intercalation and deintercalation processes, respectively [13]. The CV curves progressively increased in current response with higher scan rates and polarization voltages. Notably, when the scan rate was increased from 0.1 mV s^{-1} to 1.0 mV s^{-1}, the CV curves exhibited relatively good overlap, indicating the excellent reversibility and cycling stability of the V_2O_5@PDA electrode. This demonstrates that the electrode maintains its electrochemical performance across varying scan rates, confirming its reliability as an electrode material. Furthermore, the relationship between the scan rate (v) and peak current (i) has been established:

$$i = av^{b} \tag{1}$$

The calculation of the b-value provides a qualitative assessment of the response kinetics. Typically, the b-value ranges between 0.5 and 1.0. A b-value of 0.5 indicates a diffusion-limited process, while a value equal to 1 suggests a surface capacitive process [14]. In **Figure 5(b)**, the two redox peaks were analyzed by plotting log(i) vs. log(v). The results show that the slopes (b-values) for Peak 1 (anodic peak) and Peak 2 (cathodic peak) are 0.6023 and 0.6658, respectively. Both slopes are closer to 0.5, indicating that the electrochemical process is predominantly governed by surface-controlled capacitive behavior rather than diffusion control. This finding highlights the dominant role of rapid charge-discharge characteristics at the electrode surface throughout the reaction.

$$i(V) = k_1 v + k_2 v^{1/2} \tag{2}$$

Formula (2) quantifies the proportion of surface capacitive contributions at varying scan rates by calculating the ratio of the integrated area between the surface capacitive current and the total current. As the scan rate increases from 0.1 mV s^{-1} to 1 mV s^{-1}, the capacitive contribution proportion rises progressively from 56.9% to 81.8% (**Figure 5(c)**), demonstrating dominant pseudocapacitive behavior and accelerated Zn^{2+} intercalation/deintercalation kinetics at the material surface compared to bulk-phase reactions. This demonstrates the material's high pseudocapacitance. The increasing capacitive contribution with scan rate shows its surface can adapt to charge exchange at different rates via fast redox reactions, indicating good electrochemical performance and providing strong support for efficient energy storage and conversion in practical applications. Further analysis at 0.8 mV s^{-1} (**Figure 5(d)**) reveals that 91.44% of the total stored charge originates from surface adsorption-controlled processes, as indicated by the deep blue shaded area [15]. Thanks to its high pseudocapacitance contribution, the material's surface can facilitate rapid redox reactions, enabling valence-state changes and delivering a higher energy density. Nyquist plots (**Figure 5(e)**) exhibit a semicircle in the high-to-medium frequency range and a 45° sloped line in the low-frequency region, where V_2O_5@PDA displays a significantly reduced charge transfer resistance 130 Ω compared to pure V_2O_5 (223 Ω), along with a steeper EIS slope, confirming enhanced zinc-ion diffusion efficiency. The low-frequency sloped line corresponds to Warburg impedance, reflecting ion diffusion dynamics in the cathode: a slope of 1 indicates diffusion-controlled behavior, a slope approaching infinity signifies capacitive dominance, and intermediate slopes correlate with faster diffusion kinetics. During discharge, the gradual decrease in slope highlights slower diffusion kinetics at higher discharge depths. Both charge transfer resistance and Warburg impedance, components of Faradaic impedance, collectively validate the optimized charge transfer and reaction kinetics in V_2O_5@PDA.

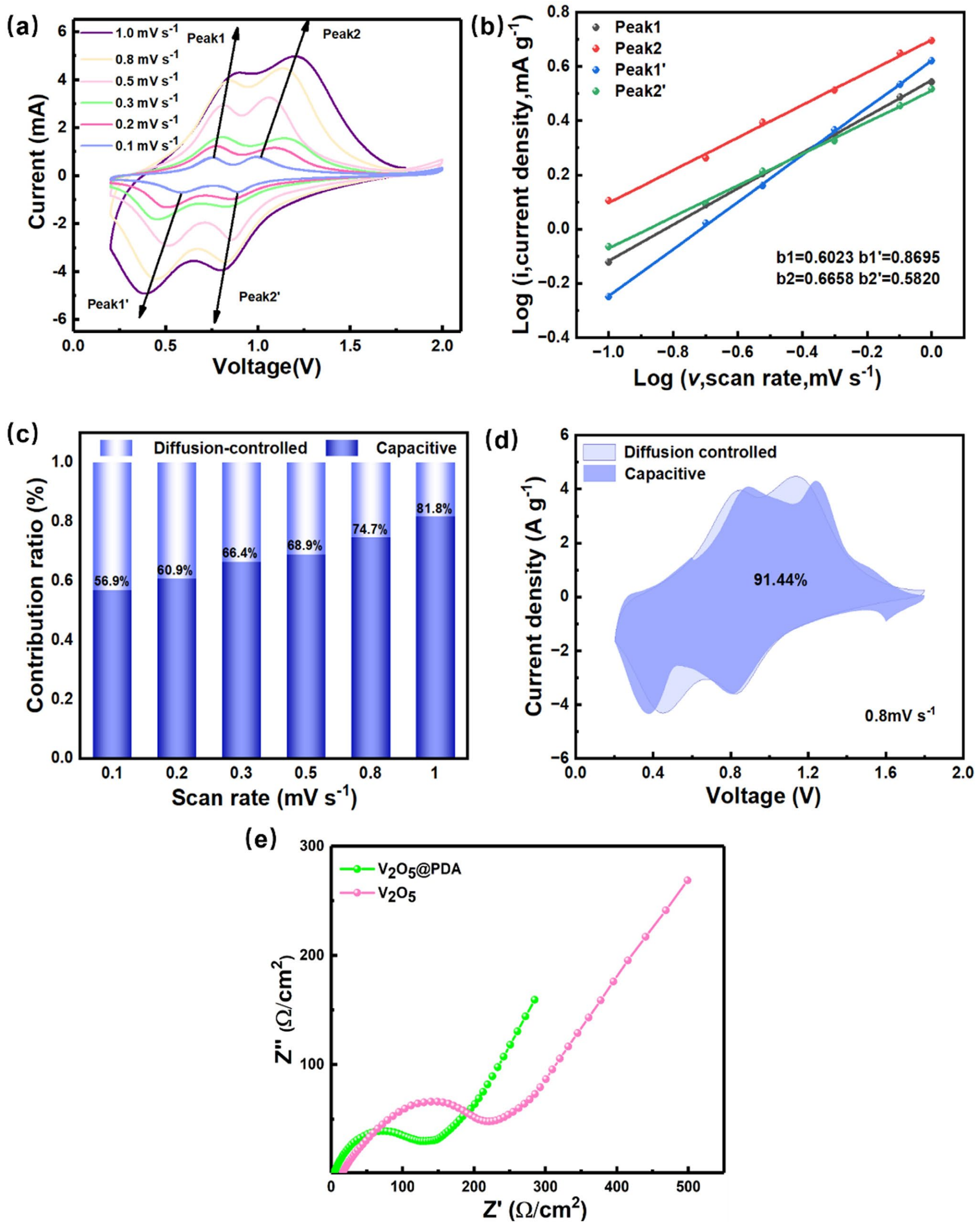

Figure 5. (a) CV curves at different scan rates; (b) Relationship between peak current and scan rate; (c) Capacity contributions from diffusion-controlled and capacitive processes at different scan rates; (d) Pseudocapacitive contribution ratio of V_2O_5@PDA at a scan rate of 0.8 mV s^{-1}; (e)Impedance comparison diagram of V_2O_5@PDA and V_2O_5.

4. Conclusion

In summary, this study successfully prepared carbon-coated V_2O_5@PDA materials through hydrothermal synthesis and atmosphere annealing methods. The formed spherical carbon-coated structure provides a larger specific surface area to increase Zn^{2+} storage sites, while the PDA serves as diffusion channels to reduce ion diffusion resistance within the V_2O_5 matrix, thereby accelerating ion reaction kinetics. Additionally, the external carbon layer effectively mitigates structural collapse during cycling and suppresses side reactions, significantly enhancing the battery's cycling stability. Experimental results further demonstrate the structural impact on battery performance, showing a high-capacity retention rate of 62.18% after 1000 cycles at 1 A g^{-1} current density. This highlights the potential of such surface modification engineering for improving AZIBs and offers an effective strategy for modifying cathode materials in AZIBs.

Acknowledgements

This research was financially supported by National Natural Science Foundation of China (No. 12164014), Guangxi Natural Science Foundation (No. 2022GXNSFAA035551).

Conflicts of Interest

The author declares no conflicts of interest regarding the publication of this paper.

References

[1] Wang, Z. and Zhu, J. (2024) Recent Advances on Stretchable Aqueous Zinc-Ion Batteries for Wearable Electronics. *Small*, **20**, Article ID: 2311012. https://doi.org/10.1002/smll.202311012

[2] Sambandam, B., Mathew, V., Ahmad Nurul, F., Kim, S., Song, M. and Kim, J. (2024) Aqueous Rechargeable Zinc-Metal Batteries: A Critical Analysis. *ACS Energy Letters*, **9**, 3058-3065. https://doi.org/10.1021/acsenergylett.4c00792

[3] Wang, Q., Wu, J., Wang, M., Yu, H., Qiu, X. and Chen, W. (2024) Vanadate-Based Fibrous Electrode Materials for High Performance Aqueous Zinc Ion Batteries. *Advanced Science*, **11**, Article ID: 2307872. https://doi.org/10.1002/advs.202307872

[4] Wu, Z., Huang, Z., Zhang, R., Hou, Y. and Zhi, C. (2024) Aqueous Electrolyte Additives for Zinc-Ion Batteries. *International Journal of Extreme Manufacturing*, **6**, Article ID: 062002. https://doi.org/10.1088/2631-7990/ad65ca

[5] Chen, M., Zhang, S., Zou, Z., Zhong, S., Ling, W., Geng, J., *et al.* (2023) Review of Vanadium-Based Oxide Cathodes as Aqueous Zinc-Ion Batteries. *Rare Metals*, **42**, 2868-2905. https://doi.org/10.1007/s12598-023-02303-2

[6] Shen, S., Li, Y., Dong, Y., Hu, J., Chen, Y., Li, D., *et al.* (2024) Vanadium Oxide Cathode Coinserted by Ni^{2+} and NH_4^+ for High-Performance Aqueous Zinc-Ion Batteries. *ACS Applied Materials & Interfaces*, **16**, 8922-8929. https://doi.org/10.1021/acsami.3c18754

[7] Chen, X., Kong, Q., Wu, X., An, X., Zhang, J., Wang, Q., *et al.* (2023) V_2O_3@C Optimized by Carbon Regulation Strategy for Ultra Long-Life Aqueous Zinc-Ion Batteries. *Chemical Engineering Journal*, **451**, Article ID: 138765.

https://doi.org/10.1016/j.cej.2022.138765

[8] Qin, X., Wang, X., Sun, J., Lu, Q., Omar, A. and Mikhailova, D. (2020) Polypyrrole Wrapped V_2O_5 Nanowires Composite for Advanced Aqueous Zinc-Ion Batteries. *Frontiers in Energy Research*, **8**, Article 199. https://doi.org/10.3389/fenrg.2020.00199

[9] Ma, Q., Gao, R., Liu, Y., Dou, H., Zheng, Y., Or, T., *et al.* (2022) Regulation of Outer Solvation Shell toward Superior Low-Temperature Aqueous Zinc-Ion Batteries. *Advanced Materials*, **34**, Article ID: 2207344. https://doi.org/10.1002/adma.202207344

[10] Chen, X., Zhang, H., Liu, J., Gao, Y., Cao, X., Zhan, C., *et al.* (2022) Vanadium-Based Cathodes for Aqueous Zinc-Ion Batteries: Mechanism, Design Strategies and Challenges. *Energy Storage Materials*, **50**, 21-46. https://doi.org/10.1016/j.ensm.2022.04.040

[11] Gonçalves, J.M. and Ruiz-Montoya, J.G. (2023) Emerging High-Entropy Coordination Compounds and Their Derivatives for Energy Application. *Journal of Materials Chemistry A*, **11**, 20872-20885. https://doi.org/10.1039/d3ta03500j

[12] Hu, B., Li, D., Li, M., Jiang, J., Zou, Y., Deng, Y., *et al.* (2025) Conductive Network Enhanced Self-Assembled Diphasic Prussian Blue Analogs for Aqueous Zinc-Ion Batteries. *Journal of Materials Chemistry C*, **13**, 6736-6744. https://doi.org/10.1039/d4tc05159a

[13] Liu, T., Xu, Z., Chen, L., Zhang, Y., Wang, M., Jia, Y., *et al.* (2022) Boosting Zinc Ion Storage Performance of Sandwich-Like V_2O_5/Graphene Composite by Effectively Inhibiting Vanadium Dissolution. *Journal of Colloid and Interface Science*, **613**, 524-535. https://doi.org/10.1016/j.jcis.2022.01.057

[14] Sun, R., Luo, D., Zhou, H., Zhang, Z., Gao, Y., Ma, S., *et al.* (2025) Synchronous Regulation of V_2O_5 Cathode and Zn Anode Using Sodium Gluconate as an Additive for Long-Life Aqueous Zinc-Ion Batteries. *Journal of Energy Chemistry*, **103**, 703-713. https://doi.org/10.1016/j.jechem.2024.12.032

[15] Ran, K., Chen, Q., Song, F. and Yang, F. (2024) Defective Construction of Vanadium-Based Cathode Materials for High-Rate Long-Cycle Aqueous Zinc Ion Batteries. *Journal of Colloid and Interface Science*, **653**, 673-686. https://doi.org/10.1016/j.jcis.2023.09.102